Facile Aqueous Solution-Gel route toward Thin Film CuBi2O4 Photocathodes for Solar Hydrogen Production

Peer-reviewed author version

JOOS, Bjorn; ELEN, Ken; VAN DEN HAM, Jonathan; Meulendijks, Nicole; BUSKENS, Pascal; PAULUS, Andreas; WOUTERS, Koen; MANCA, Jean; D'HAEN, Jan; SHUKLA, Sudhanshu; VERMANG, Bart; VAN BAEL, Marlies & HARDY, An
(2023) Facile Aqueous Solution-Gel route toward Thin Film CuBi2O4 Photocathodes for Solar Hydrogen Production. In: Advanced Sustainable Systems, 7 (8) (Art N° 2300083).

DOI: 10.1002/adsu.202300083
Handle: http://hdl.handle.net/1942/40232

Facile aqueous solution-gel route towards thin film $CuBi_2O_4$ photocathodes for solar hydrogen production

Bjorn Joos[1,5,7], Ken Elen[1,5,7], Jonathan van den Ham[6], Nicole Meulendijks[6], Pascal Buskens[1,6], Andreas Paulus[1,5,7], Koen Wouters[4], Jean Manca[4], Jan D'Haen[2], Sudhanshu Shukla[3,5,7], Bart Vermang[3,5,7], Marlies Van Bael[1,5,7], An Hardy[1,5,7]

1 UHasselt - Hasselt University, Institute for materials research (imo-imomec), DESINe, Martelarenlaan 42, 3500 Hasselt, Belgium

2 UHasselt - Hasselt University, Institute for materials research (imo-imomec), AMS, Martelarenlaan 42, 3500 Hasselt, Belgium.

3 UHasselt - Hasselt University, Institute for materials research (imo-imomec), TFPV, Materlarenlaan 42, 3500, Hasselt, Belgium

4 UHasselt - Hasselt University, X-LAB, Agoralaan – Gebouw D, B-3590 Diepenbeek, Belgium

5 imec Division imomec (Partner in Solliance), Wetenschapspark 1, B-3590 Diepenbeek, Belgium

6 The Netherlands Organisation for Applied Scientific Research (TNO), High Tech Campus 25, 5656AE Eindhoven, The Netherlands

7 EnergyVille, Thor Park 8320, 3600 Genk, Belgium

ABSTRACT

A new benign aqueous route towards bismuth-containing photoelectrodes is proposed to eliminate the need for harmful organic solvents and/or acids. A $CuBi_2O_4$ photocathode was prepared by stabilizing the metal ions through complexation in pH neutral aqueous solutions. Merits of the proposed approach are elemental homogeneity (with unique doping possibilities) and ease of fabrication (*e.g.* high scalability). The prepared aqueous $CuBi_2O_4$ precursor forms a nearly phase-pure kusachiite crystalline phase free of organics residuals and capable of water reduction due to its sufficiently negatively positioned conduction band at -0.4 V vs. RHE. Deposition on FTO/glass substrates and thermal treatment leads to uniform but granular films of $CuBi_2O_4$ with excellent control over stoichiometry and thickness, owing to the facile and non-destructive synthesis conditions. Ultimately, the optimized $CuBi_2O_4$ photocathodes produced AM1.5G photocurrent densities of up to -1.02 $mA \cdot cm^{-2}$ at 0.4 V vs. RHE with H_2O_2 as an electron scavenger, competing with bare $CuBi_2O_4$ prepared through less benign non-aqueous organic synthesis routes.

INTRODUCTION

The production of hydrogen by means of renewable energy sources has been of great interest to the scientific community and industry. Indirect utilization of solar energy by means of photovoltaics and an electrolyser is reaching technological maturity levels.[1] Instead, the direct storage of solar energy into hydrogen is still under development. Here, photoelectrochemical water splitting (PEC) is performed by production of hydrogen and oxygen at the (photo)electrodes.[2, 3] The latter are submerged in an aqueous electrolyte and generate sufficient potentials for hydrogen and/or oxygen generation upon illumination. Adequate photoelectrodes fulfil certain energetic requirements. First, photoelectrodes should generate a sufficient photovoltage as driving force for the splitting of water.[3] The thermodynamics of water splitting dictate a potential difference of 1.23 V but various sources of overpotential and kinetic losses during charge carrier transport (*e.g.* recombination or ohmic losses in

the external circuit) lead to an overall potential difference of 1.8-1.9 V to drive water splitting.[2] Secondly, semiconductor photoelectrodes require conduction and/or valence band edges at a suitable position to drive the hydrogen and/or oxygen evolution reaction, respectively.[2, 3] Ideally, it is desirable to have photoelectrodes consisting of abundant, completely non-toxic, low-cost, non-critical elements. Other requirements include a high (photo)chemical stability, high photocurrent, and high minority carrier diffusion length, among many others.[2, 3]

Hence, the ideal photoelectrode will be able to absorb a large fraction of the incident solar radiation and store the energy in the form of hydrogen, with a high solar-to-hydrogen (STH) efficiency, over a long lifetime.[2] Various semiconductors have been applied for solar water splitting but we refer to excellent reviews in the literature, and provide a few highlights in this fascinating field.[3, 4] The III-V semiconductors (*e.g.* GaAs and InP) and perovskite semiconductors (*e.g.* $CH_3NH_3PbI_3$, $(Cs_{0.15}FA_{0.65}MA_{0.20})Pb(I_{0.8}Br_{0.2})_3$) are well known candidates from photovoltaics (PV).[5-9] These semiconductors are highly efficient but consist of highly toxic, costly, and non-abundant elements and are chemically unstable against aqueous solutions.[3] Typically, they are buried and merely generate the necessary electric field in the photoelectrode, in so-called PV-PEC devices. A champion buried III-V based device was proposed by Cheng et al., *i.e.* $Rh/TiO_2/AlInPOx/AlInP/GaInAs/GaAs/RuO_x$ device, demonstrating a STH of 19.3%.[5] Chalcogenide semiconductors, *e.g.* Sb_2Se_3, $Cu_2ZnSn(S,Se)_4$, Cu_2CdSnS_4 and Cu_3BiS_3, are another promising class, only mildly toxic and more earth-abundant.[10-18] The Sb_2Se_3 is stable in neutral and basic aqueous solutions, even in acidic conditions upon protection with MoS_x.[10, 15] Half-cell STHs of Sb_2Se_3 and $Cu_2ZnSn(S,Se)_4$ are reported to reach 4.7% and 6.47% respectively.[11, 14, 19]

Metal oxide semiconductors fulfil most of the listed criteria and have been at the forefront for decades.[3] Common materials include n-type TiO_2, α-Fe_2O_3, $BiWO_4$ as a photoanode and p-type Cu_2O as a photocathode. The p-type semiconducting $CuBi_2O_4$ (CBO) has been identified as a promising metal oxide photocathode with a suitable band gap of 1.5-1.9 eV and an aptly aligned conduction band edge for the hydrogen evolution reaction (HER).[20-28] An internal photovoltage of ~ 1 V is plausible from CBO photocathodes. A PEC stack is envisaged by coupling CBO with suitable photoanode or providing external bias of ~0.2-0.3 V.[29, 30] The preparation of p-type $CuBi_2O_4$ has been well-reported in literature through various methods such as electrodeposition, pulsed laser deposition (PLD), drop-casting, RF-magnetic sputtering, spin-coating, hydrothermal growth, etc.[20-27, 31-33] Solution-based approaches are ideal for the scale-up of deposition processes. However, the facile, scalable, and green aqueous deposition of thin-film $CuBi_2O_4$ is hampered by the solubility of bismuth in water.[23, 34] In contrast to Cu^{2+} salts, Bi^{3+} salts are only water soluble in acidic conditions. The high valent Bi^{3+} is prone to hydrolysis, forming insoluble (hydr)oxides, e.g. the solubility of bismuth citrate in water at neutral pH is below 54 mg l^{-1} at 20°C, insufficient for facile solution processing.[35, 36] Hence, the few reported aqueous routes typically occur through electroplating of acidic Bi^{3+} solutions to deposit Bi.[22, 23, 26, 37, 38] Unfortunately, Bi metal itself is soluble in aqueous acidic solutions, which leads to leaching upon lifting the cathodic protection and hinders the deposition of uniform films. This is mostly of concern on non-metallic back electrodes where the Bi-substrate bond is rather weak, e.g. with transparent conducting oxides (TCOs) such as indium doped tin oxide (ITO) and fluorine doped tin oxide (FTO).[23] Several other aqueous solution-based coating approaches, e.g. spin-coating, drop-casting, blade-coating, spray-coating, etc., of acidic Bi^{3+} solutions face challenges as thicker films are prepared by multiple subsequent depositions. The acidic Bi^{3+} solution of the subsequent deposition could alter/dissolve the pre-deposited material. Hence, the use of organic solvents such as acetic acid and ethanol persists.[20, 27] Van de Krol *et al*. demonstrated that the thickness of the deposited $CuBi_2O_4$ layers increases linearly upon additional drop-casts with the use of such organic solvents.[20] However, the use of aqueous solution-based approaches have been sparingly reported.[25, 28, 39, 40] For instance, the work of Chu *et al.* describes the

preparation of $CuBi_2O_4$ powders in an aqueous nitric acid solution while Hofmann *et al.* describe the thin-film deposition of $CuBi_2O_4$ in a mixture of water, acetic acid and 2-methoxyethanol.[25, 28] Both reports used citric acid as a gelling agent but acidic conditions were maintained in the precursors as to stabilize the Bi^{3+}.

Aqueous routes are of interest as to omit the use and need of harmful organic solvents, yet did not render the need for acidic conditions redundant. No work has described the deposition of $CuBi_2O_4$ through a pH neutral aqueous medium to the best of our knowledge. Hence, in this work we set out to investigate and expand the aqueous solution-based routes to benign and pH-neutral conditions by means of citrato-ligand based solution-gel chemistry. Within our research group, several stable pH-neutral metal ion precursors have been prepared by the use of complexes.[36, 41-49] For instance, Marchal *et al.* reported the preparation of self-reducing copper-formate-amine complexes.[50] Meanwhile, Nelis *et al.* reported the stabilized Bi^{3+} metal ion precursor.[49] The preparation of multimetal oxides facilitated by such stable solutions, e.g. $Bi_4Ti_3O_{12}$, $SrBi_2Nb_2O_9$, has been demonstrated numerously. The facile mixing of stable monometal ion precursors in the appropriate ratios allows us to easily deposit and obtain the desired multimetal oxide. Hence, we believe that the synthesis procedure proposed in this manuscript not only is a highly flexible, green, and facile route towards $CuBi_2O_4$ but it can be extended towards other metal oxide photoelectrodes such as Bi_2WO_6, $CuFe_2O_4$, etc. As such, it can be extended as a general strategy towards the greener fabrication of said oxide-based materials family.

EXPERIMENTAL SECTION

MATERIALS Bismuth(III)citrate (99.99% trace metals basis, -325 mesh) Aldrich, ethanolamine (99+%) VWR, copper(II)formate tetrahydrate (≥98%) VWR, ammonia solution (32%) VWR, citric acid (99%) Sigma Aldrich, monopotassium phosphate (≥99.5%) Merck, dipotassium phosphate trihydrate (>99%) Merck, potassium sulfate (99+%) Acros, hydrogen peroxide (35%, stabilized) Merck. These products were used as received. Fluorine doped tin oxide ($F:SnO_2$) coated glass slides (electrical resistivity ρ = 7 Ω/sq) were used as a substrate to deposit the metal oxide thin films and was obtained from Sigma Aldrich. Quartz substrates were obtained from Glasatelier Saillard (Belgium).

PREPARATION OF METAL PRECURSORS The preparation of the aqueous bismuth precursor is described in detail in our previous work.[43, 49] First, an appropriate amount of bismuth(III)citrate was dissolved in Milli-Q water and monoethanolamine (MEA) was added in a molar ratio 1:1.5 of Bi:MEA leading to a transparent slightly yellowish solution. Then ammonia was added to increase the pH to 7.0 and obtain the final bismuth precursor with concentration of approximately 1.3 M. The aqueous copper precursor was made similarly to the bismuth precursor. First copper(II)formate tetrahydrate was dissolved in Milli-Q water, then citric acid (CA) is added in a 1:1 molar ratio of Cu:CA. Lastly, ammonia was added to deprotonate the CA and increase the pH to 7.0. Finally, a deep blue copper precursor with concentration of approximately 1.1 M was obtained. The multimetal ion precursor was prepared by mixing the Cu and Bi precursors in the appropriate ratio, to obtain a molar ratio of 1:2 of Cu:Bi. Lastly, Milli-Q water was added to dilute the precursors to an appropriate metal ion concentration, i.e. 0.5 M.

PREPARATION OF THE METAL OXIDE POWDER The multimetal ion precursor was transferred into a Petri dish and kept at 80°C for 16 hours in an oven to evaporate the water solvent and to obtain a transparent blue gel. The gel is pre-calcined at 200°C under air for 30 hours to obtain a Cu/Bi cake and to allow the thermal breakdown of the ligands and emission of volatiles. Lastly, the pre-calcined powders were calcined and annealed for 2 hours in a muffle furnace in air to obtain the metal oxide.

The muffle furnace is heated to either 480°C, 540°C, or 600°C at a rate of 10°C·min^{-1} and allowed to cooldown naturally after 2 hours.

DEPOSITION OF THE METAL OXIDE PRECURSOR The substrates were cleaned according to a standard procedure.[51] They were submerged and sonicated for 10 minutes in deionized water, acetone, and iso-propanol sequentially. Then they received 30 minutes of UV/O_3 treatment to remove any surface contaminations. The multimetal ion precursor was deposited through spin-coating. First, 0.3 ml of the multimetal precursor was applied on a 4 cm² (2x2) substrate by means of a syringe with a 0.2 µm Acrodisc filter. Next, the substrate was spun at 3000 rpm for 30 seconds. Hereafter, three subsequent heating steps were applied to remove the solvent and organics and to form and crystallise the deposited metal oxide under air. The coated substrate was consecutively held for 1 minute at 110°C, 2 minutes at 270°C, and 2 minutes at 480°C on a hot plate without cooldown periods. The deposition protocol was repeated for a certain number of times, so as to prepare multi-layered films with an increasing thickness (vide infra). Lastly, the complete stack was annealed for a prolonged time (2 hours) on the hot plate at selected temperatures (480, 540 or 600°C).

CHARACTERIZATION *(Physico)chemical characterization.* Powder X-ray diffraction (PXRD) and Film XRD were carried out with a Bruker D8 Advance equipped with Lynxeye detector and operated with Cu $K_{\alpha1}/K_{\alpha2}$ radiation to identify the crystalline phases of the CBO powders and films. The powders and films were further analysed by means of Raman spectroscopy performed on a Horiba Jobin-Yvon T64000 spectrometer, equipped with a Symphony detector and a 100x Olympus objective. The 488 nm Lexel SHG laser was operated at a power of less than 20mW. Thermogravimetric analysis was carried out on a Q500 TA Instrument TGA from room temperature to 800°C with a heating rate of 10°C min^{-1} under dry air or oxygen flow at 60 ml min^{-1}. Organic moieties in the powders were identified by means of an attenuated total reflectance Fourier-transform infrared spectroscopy (ATR FT-IR, Perkin Elmer-Frontier, range 4000-400 cm^{-1}, resolution 1 cm^{-1}) with the MIRacle single reflection ATR accessory. The elemental composition of the powders and the deposited films was analysed by means of inductively coupled plasma atomic emission spectroscopy (ICP-AES) after dissolution in an aqueous 5 wt% nitric acid solution. A Thermo Electron Flash EA1112 elemental analyzer (ThermoFisher Scientific, Waltham, USA) was used to determine total carbon content of all powder samples. Calibration was performed using BBOT ((2,5-bis (5-tert-butyl-benzoxazol-2-yl) thio-phene) (pure, ThermoScientific). Scanning electron microscopy (SEM) measurements were carried out on a Zeiss 450 Gemini 2 FEG-SEM (Oberkochen, Germany). Atomic force microscopy (AFM) measurements were carried out with a Bruker Multimode 8 microscope in the peak-force Quantum nanomechanical (PF-QNM) mode. The probe used during imaging (RTESPA, supplied by Bruker) contained a rectangular cantilever with a pyramidal tip with a nominal tip radius of 8 nm. AFM data were processed with Gwyddion software, topography images were flattened by using plane levelling, and the roughness was calculated using the statistical quantities tool.[52] Thickness measurements were performed with a Bruker DektakXT profilometer after etching a small section of the deposited CBO thin film by means of an 5% nitric acid aqueous solution. Optical transmittance *T*(%) and reflectance *R*(%) spectra of the CBO films were measured on a Cary 5000 UV-VIS-NIT spectrophotometer (Agilent Technologies) with an integrating sphere. The latter is used to calculate the optical absorptance *A*(%) and the absorption coefficient α (cm^{-1}) by utilizing Equation 1 and Equation 2 below with *t* as the layer thickness (cm) as determined from profilometer measurements.[20]

Equation 1 $$A(\%) = 100\% - T(\%) - R(\%)$$

Equation 2 $$\alpha\ (cm^{-1}) = \frac{1}{t\ (cm)} \cdot ln(\frac{100 - R(\%)}{T(\%)})$$

PHOTOELECTROCHEMICAL CHARACTERIZATION The electrolytes were prepared by mixing an aqueous 0.2M solution of KH_2PO_4 solution and an aqueous 0.2M K_2HPO_4 in equal portions to obtain the 0.2M phosphate buffer. Herein 0.3M K_2SO_4 was dissolved and the pH was measured to be 6.85. Another electrolyte was prepared similarly with 0.25M phosphate buffer and 0.375M K_2SO_4, which is then diluted in a volume ratio of 4 to 1 with H_2O_2 (30%).

Photocurrent measurements were performed with a Redox.me LED solar simulator (AAA). The lamp is calibrated to 100 mW/cm² and matches the AM1.5G spectrum. The electrolyte with H_2O_2 was used to scavenge the electrons from surface state traps. The $CuBi_2O_4$ thin film sample was placed in a two-chamber measurement cell (Redox.me PECF H-cell 2x1.5ml with a 1 cm² opening). A Pt wire with excess surface area was used as the counter electrode and an Ag/AgCl (3.0M KCl) electrode as the reference electrode. A Metrohm PGSTAT128N potentiostat was used to bias the cell. So, all the experimentally determined potentials were converted to the V vs. RHE scale with Equation 3.[2]

Equation 3 $$E\ (vs. RHE) = E\ (vs.\ Ag/AgCl) + 0.210 + 0.0591 \cdot pH$$

Mott-Schottky graphs were determined by electrochemical impedance spectroscopy measurements using the Metrohm PGSTAT128N potentiostat with the $CuBi_2O_4$ thin film sample placed in a two-chamber measurement cell (Redox.me PECF H-cell 2x1.5ml with a 1 cm² opening). The H_2O_2 free electrolyte was used and Equation 4, with C the areal capacitance ($F \cdot m^{-2}$), ε_0 the permittivity of vacuum ($F \cdot m^{-1}$), ε the relative permittivity of $CuBi_2O_4$, N_A the acceptor density (cm^{-3}), ϕ_{FB} the flat band potential (V), ϕ the applied bias potential (V), k the Boltzmann constant ($eV \cdot K^{-1}$), and e the elementary charge. The relative permittivity ε was set at 80 as suggested by Klyndyuk *et al.*[53] The capacitance was extracted by fitting the obtained impedances with the Randles equivalent circuit model, see **Figure S10** in the Supplementary Information. The exposed surface area of the $CuBi_2O_4$ to the electrolyte was estimated with SEM and AFM, and used to calculate the areal capacitance C. Mott-Schottky analysis were performed using the classical relationship for p-type semiconductor given below.[2, 54, 55]

Equation 4 $$\frac{1}{C^2} = \frac{2}{e\varepsilon\varepsilon_0 N_A}\left(\phi_{FB} - \phi - \frac{kT}{e}\right)$$

The valence band and conduction band edges, in either energy (eV vs. vacuum) or potential (V vs. RHE), were estimated by means of Equation 6 and Equation 7. The Fermi level E_F, bandgap E_g, and acceptor density N_A obtained from the Mott-Schottky and UV-VIS measurements. The electron charge is equal to negative the elementary charge e.[54] Lastly, the space charge layer thickness D (nm) was then calculated with Equation 7.[2]

Equation 5 $$E_F - E_V = (U_F - U_V) \cdot -e = -\frac{kT}{e} ln\left(\frac{N_A}{N_V}\right)$$

Equation 6 $$E_C - E_V = (U_C - U_V) \cdot -e = E_g$$

Equation 7 $$D = \sqrt{\frac{2\varepsilon\varepsilon_0}{eN_A}\left(\phi_{FB} - \phi - \frac{kT}{e}\right)}$$

RESULTS AND DISCUSSION

The aqueous bismuth monometal ion precursor is obtained by the dissolution of bismuth citrate in Milli-Q water along with monoethanolamine (1.5:1 molar ratio to bismuth citrate) and neutralization of the pH with ammonia, see **Figure S1** in Supplementary Information.[43] The monoethanolamine ensures the stability of the Bi monometal ion precursor.[43] Over the course of a few hours, the bismuth salt dissolves and forms a clear faint-yellow solution. The copper monometal ion precursor is prepared in a similar fashion but copper (II) formate tetrahydrate is used, as commercial copper (II) citrate is unavailable, see **Figure S1** in Supplementary Information. The dissolution of copper is evident from the immediate blue coloration of the solution yet some precipitate remains.[56] Subsequently, citric acid is added in a 1:1 molar ratio, which allows the full dissolution of the copper (II) formate, and the pH is adjusted to 7 by means of ammonia. The addition of ammonia leads to ligand exchange, as the blue coloration deepens significantly as a result from the higher ligand field. Both monometal ion precursors are filtered (Acrodisc < 0.2 µm) and remain stable, over the course of more than one year, with no formation of precipitate. Both monometal ion precursors are prepared as such to obtain a high metal ion concentration, approximately 1.1 to 1.3 M, for Cu and Bi respectively, as confirmed by Inductively Coupled Plasma - Atomic Emission Spectroscopy (ICP-AES).

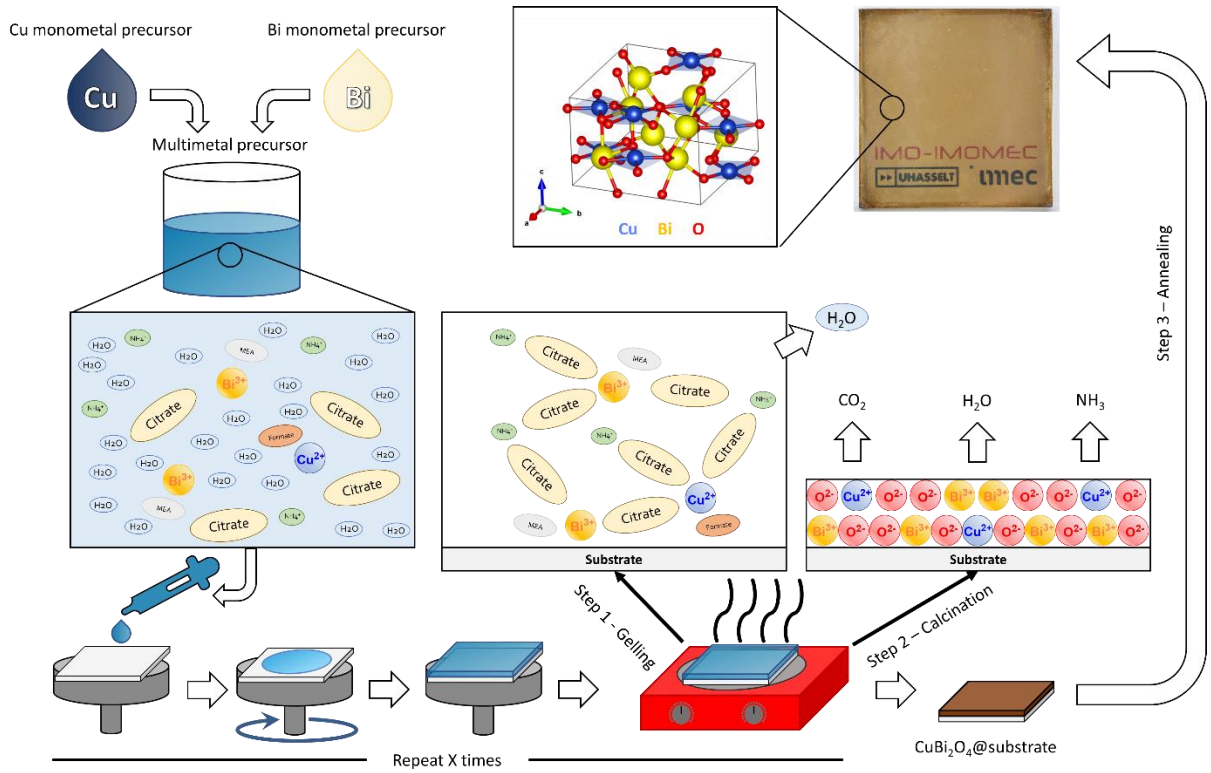

Figure 1. The synthesis route for the deposition of $CuBi_2O_4$ kusachiite on the substrate by means of an aqueous solution-gel route. First the multimetal ion precursor is prepared from the Cu and Bi monometal ion precursors in a stoichiometric ratio. Next, the multimetal ion precursor is deposited on the substrate by means of spin-coating, and undergoes a two-step heat treatment to allow gellification and calcination. The deposition is repeated several times to obtain a $CuBi_2O_4$ kusachiite film of desirable thickness, which is then annealed. An optical image of a sample, five layers of $CuBi_2O_4$ on an FTO/glass substrate, on top of a white background with our institute's logo is given to demonstrate the transparency.

The multimetal ion precursor can be prepared easily by the mixing of the monometal ion precursors in an appropriate molar ratio, i.e. in view of $CuBi_2O_4$ a Cu:Bi ratio of 1:2 is used, see **Figure 1**. The

multimetal ion precursor remains stable and does not yield any visual precipitation for at least one year. The deposition of the Cu/Bi oxide is carried out by means of spin-coating on transparent conductive oxides (TCO, F:SnO_2 coated on glass) for its use as a photocathode. But first, the ability of the multimetal ion precursor to form a phase-pure crystalline $CuBi_2O_4$ is evaluated by the preparation of Cu/Bi oxide powders.

The multimetal ion precursor was transferred into an open vessel and heated at 80°C overnight to remove the solvent and form a clear blue transparent gel, see **Figure S2 i**n the Supplementary Information. The latter gel consists of a three-dimensional network with a homogeneous distribution of the Cu^{2+}, Bi^{3+}, and NH_4^+ cations, which act as coordination centres for the bridging tridentate citrate ligands, see **Figure 1**. For a deeper insight into this gel formation, we refer to the previous works within our group.[36, 41-46, 48, 49] Essentially, the homogeneous elemental distribution is one of the virtues of the proposed solution-gel approach. It allows for control of stoichiometry and the facile introduction of dopants, which can alter the properties of the semiconductor whereas depositions methods such as pulse layer deposition (PLD), chemical vapor deposition (CVD), and solid-state synthesis require meticulous control of the reagents and processing conditions.[21] Ultimately, the NH_4^+ and citrate ligands are removed by thermal treatment under an oxidative atmosphere, i.e. calcination, to yield the desired Cu/Bi oxide. This thermal treatment is performed in two subsequent steps, first an intermediate pre-calcination step at 200°C in a furnace under air to obtain the pre-calcined Cu/Bi cake. The intermediate heat treatment is required to facilitate the removal of the organics as the degradation of the ligands releases vast amounts of volatiles such as NH_3, CO and CO_2.[36] The latter leads to a massive volume expansion of the gel. Next, the pre-calcined Cu/Bi cake is crushed in a mortar to obtain a fine powder. Dynamic thermogravimetric analysis (TGA) under dry air flow was used to determine the required temperature for full removal of the organics present in the pre-calcined Cu/Bi powder, see **Figure 2a**. The TGA profile reveals a first minor mass loss up to 150°C, which can be ascribed to residual moisture absorbed by the pre-calcined powder through atmospheric exposure. No significant mass loss is observed up to 250°C as the powder underwent the intermediate pre-calcination heat treatment step prior to the TGA measurement. A first significant mass loss is observed between 250°C and 350°C, a second between 350°C and 420°C, and a third between 420°C and 490°C. These three peaks can be generally ascribed to the thermal oxidative breakdown of the free organics (i.e. monoethanolamine, citric acid, ammonia), complexing ligands, and remaining organics, respectively.[36, 41-46, 48, 49] No further mass loss is observed beyond the temperature of 490°C. Due to the dynamic nature of the TGA, and the kinetics of thermal decomposition, the minimal calcination temperature was set slightly lower at 480°C. For reference, this is only slightly higher than the annealing temperatures used for $CuBi_2O_4$ powders and films prepared from organic solvents.[20, 22, 23, 27]

With the thermal analysis in mind, the pre-calcined Cu/Bi powder is calcined at three different temperatures, *i.e.* 480°C, 540°C, or 600°C for two hours in a muffle furnace under air, to study the effect of the calcination temperature on the crystallisation of the Cu/Bi oxide. Elemental Carbon-Hydrogen-Nitrogen-Sulfur (CHNS) analysis confirms the near-complete loss of organics during the final calcination step, from 17.0 ± 0.3 m% carbon in the pre-calcined Cu/Bi powder to less than 0.15 ± 0.01 m%, see **Table 1**. This is further confirmed by the thermogravimetric analysis of the calcined samples where little to no mass loss is found under highly oxidative O_2 flow, see **Figure S3** in the Supplementary Information, as well as the absence of organic vibrations in ATR-FTIR signals of the calcined powders, see **Figure S4** in the Supplementary Information. The low melting temperature and high volatility of the bismuth, leading to bismuth losses and off-stoichiometry oxides in the end, is often a concern for high temperature treatments.[57, 58] Therefore, the Bi/Cu ratio in the liquid multimetal ion precursor, pre-calcined powder, and calcined powders is determined by means of ICP-AES. The (pre)calcined powders are digested in an aqueous 5 wt% nitric acid solution to solubilize the Cu and Bi ions. We

observe that the Bi/Cu ratio remains at the nominal value of 2 with no apparent loss of bismuth, see **Table 1**. Hence, the thermal and elemental analysis reveal that a nearly organic-free stoichiometric 1/2 Cu/Bi oxide can be prepared by the proposed aqueous solution gel route.

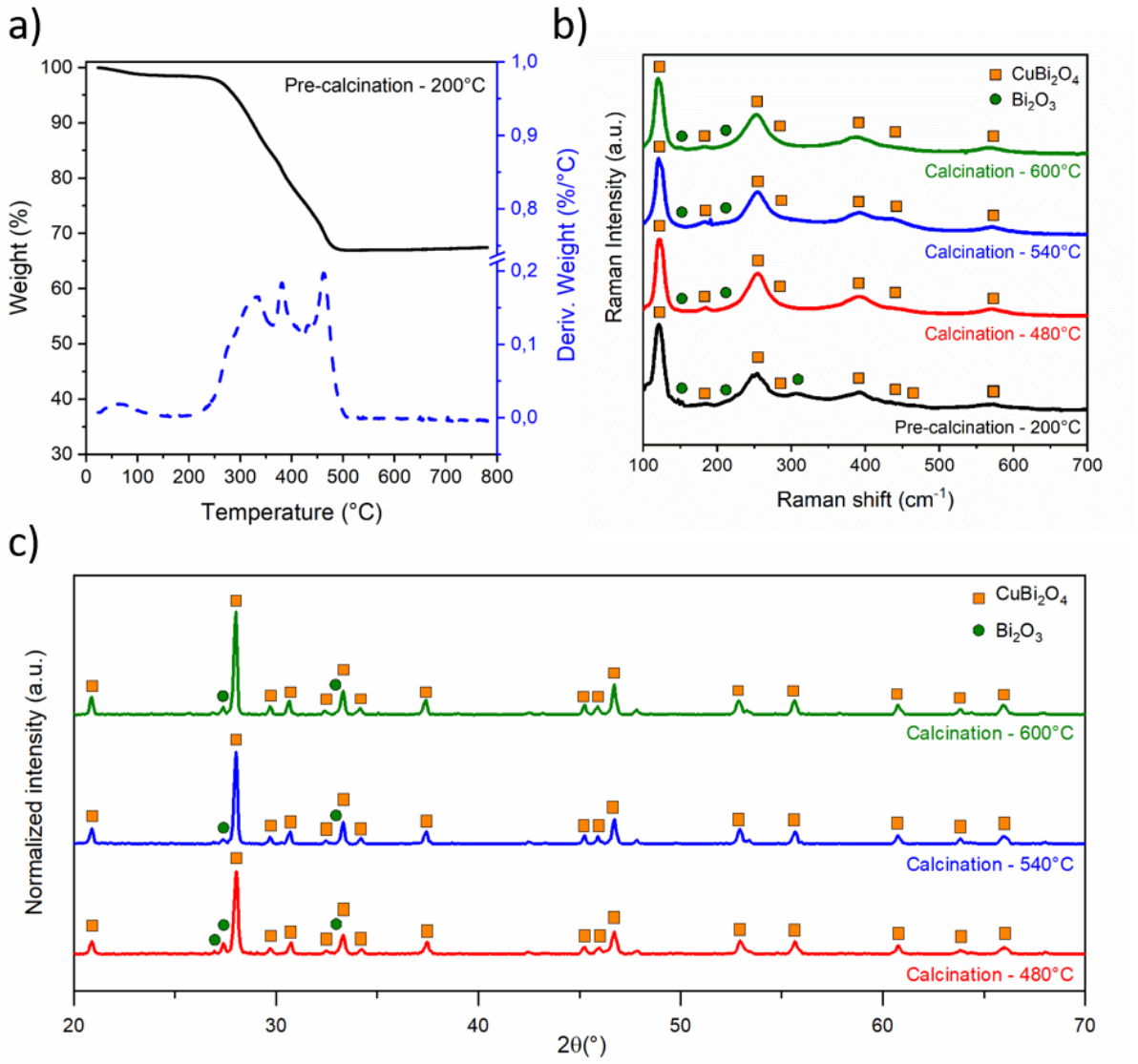

Figure 2. a) Thermogravimetric analysis of the crushed pre-calcined Cu/Bi powder under dry air flow (60 ml·min^{-1}). Heating rate was 10°C·min^{-1}. b) Raman spectra of the prepared Cu/Bi oxide powders at selected calcination temperatures. The $CuBi_2O_4$ Raman vibrations are given in orange squares while the main Bi_2O_3 Raman vibrations are given in green circles.[59, 60] c) The powder X-ray diffractograms of the Cu/Bi oxide powders calcined at 480°C, 540°C, and 600°C for two hours respectively. The $CuBi_2O_4$ diffraction peaks (COD no. 96-100-8477) are given in orange squares while the main Bi_2O_3 peaks (COD no. 96-901-2547) are given in green circles. The intensities are normalized to background noise between 38° and 44°.[53, 59-64]

Table 1. Elemental analysis by CHNS (standard deviation given), ICP-AES, and Rietveld analysis of the powder X-ray diffractograms of the liquid multimetal precursor (MuMI), pre-calcined Cu/Bi powder (200), and calcined Cu/Bi oxides at select temperatures (480, 540, and 600°C).

Sample	CHNS	ICP-AES	PXRD- Rietveld (w%)

Calc. T (°C)	Carbon w%	Bi/Cu ratio	$CuBi_2O_4$	CuO	Bi_2O_3
MuMI	N/A	2.01	N/A	N/A	N/A
200	17.0 ± 0.3	1.98	N/A	N/A	N/A
480	0.15 ± 0.01	2.02	89.2	0.4	10.4
540	0.078 ± 0.005	2.03	94.8	0.1	5.1
600	0.01 ± 0.01	2.02	92.7	0.0	7.3

The crystallinity of the Cu/Bi oxide is analysed by means of powder X-ray diffraction (PXRD), see **Figure 2c**. The main phase of the three calcined powders can be identified as the tetragonal $CuBi_2O_4$ kusachiite phase (*P4/ncc* space group), hereafter referred to as CBO.[53, 61, 62] A small fraction of crystalline monoclinic α-Bi_2O_3 bismite phase (*$P2_1/C$* space group) can be detected as well, which content seems to decrease upon increasing the annealing temperature.[65] Meanwhile, no CuO phase is readily detected in the diffractograms. Rietveld analysis was performed to estimate the mass fractions of each crystalline phase. Calcination at 540°C yields the most phase-pure CBO at approximately 95 wt%. On the basis of stoichiometry and molecular masses, we can expect 0.17 wt% CuO (M=79.5) for every 1 wt% of Bi_2O_3 (M=466) in the calcined powder. Therefore, we argue that the content of a CuO phase could simply lie below the instrument detection limit. Another plausible cause could be the high dispersion of the 'excess' Cu throughout the powder whereas bismuth, due to its low melting point at 270°C, could be reduced in-situ by the degradation of the organic ligands, melt, coalesce, and form detectable oxide crystallites upon re-oxidation. For Cu, this is impossible within the thermal window due to its high melting temperature of 1083°C. Furthermore, Raman spectroscopy is unable to confirm the presence of any disordered CuO phase either, see **Figure 2b**. Meanwhile, the spectra confirm the formation of the CBO by its four main characteristic A_{1g} Raman vibration modes at 130, 260, 400, 580 cm^{-1}, even in the pre-calcined organic-containing Cu/Bi powder, as well as some Bi_2O_3 peaks.[59, 60, 63, 64] The latter peaks overlap largely with the CBO B_{2g} and E_g vibration modes which makes it difficult to distinguish.[59] However, the B_g vibration mode at 310 cm^{-1} can unambiguously be ascribed to the Bi_2O_3 phase and vanishes upon annealing. An alternative preparation of the CBO through a Cu-rich multimetal ion precursor, i.e. Bi/Cu 1.90, still produces small contents of monoclinic Bi_2O_3 which lowers in content upon increasing the calcination temperature, see **Figure S5** in Supplementary Information. Hence, we hypothesize that during the calcination both Bi_2O_3 and CuO secondary-phases serve as intermediates, and are consumed to form CBO. Therefore, the increase of the calcination temperature facilitates the conversion of the Bi_2O_3 and CuO secondary-phases into the desired CBO.

Hence it is clear that the thermal oxidative degradation of the multimetal ion precursor can result in the formation of nearly phase-pure CBO photocathode material with full removal of the organic fraction. The optimum calcination/annealing temperature is found at 540°C, where only a minimal Bi_2O_3 residual-phase is detected. The photocathode is developed by depositing the multimetal ion precursor onto an UV-O_3 treated fluorine doped tin oxide (FTO) coated sodium borosilicate glass substrate, hereafter referred to as FTO/glass. This deposition is carried out *via* spin-coating, and subsequent thermal treatments, see **Figure 1**. The multimetal ion precursor-coated FTO/glass substrates are subjected to a multi-step thermal treatment in ambient. First, the water solvent is removed at 110°C (1 minute) to form a gel in which the metal cations are homogenously dispersed through the tridentate citrate coordinated by the ligands. Next, the calcination is performed in two intermediate steps, *i.e.* 270°C (2 minutes) and 480°C (2 minutes), to thermally break down the organic ligands and obtain the Cu/Bi oxide. This procedure is repeated several times to obtain thicker films of the Cu/Bi oxide on the FTO/glass substrate. A final annealing at either 480°C, 540°C, or 600°C (2 hours) is performed to allow the crystallization of the Cu/Bi oxide into the desired CBO kusachiite phase.

The deposition of the Cu/Bi oxide on the FTO/glass substrate yields transparent brownish films as observed in the insets in **Figure 3a** for selected films, we refer to **Figure S6** in the Supplementary Information for a full visual comparison between Cu/Bi oxide films of various thicknesses. The thickness of the Cu/Bi oxide films annealed at 540°C for two hours is evaluated by profilometer measurements. The height difference between a pristine section of the film and an etched substrate surface, by means of an aqueous nitric acid solution, is measured. The results are shown below in **Figure 3a**. We observe a linear correlation between the thickness and the number of deposited layers of the film. The thickness of each deposited layer can be estimated as approximately 34 nm per additional layer. Thus, the thickness of the deposited Cu/Bi oxide can be controlled and fine-tuned to the desired value. This precise control over thickness is enabled by the pH neutral multimetal ion precursor, whereas conventionally deployed harsh acidic conditions simply etch or alter the previously deposited layers.[22, 23, 26, 37, 38] Intuitively, the thickness of the deposited layers can be tweaked further by altering the total metal ion concentration in the multimetal ion precursor as well as the spinning-coating parameters. However, it is beyond the scope of this work. The five-layer film of the Cu/Bi oxide, with a thickness of ±170nm, on the FTO/glass was chosen as a representative model for the further characterization. The morphology of the deposited films and its dependence on the thermal annealing was further studied by means of scanning electron microscopy (SEM) and atomic force microscopy (AFM) imaging, see **Figure 4**. A uniformly continuous pin-hole free CBO film is observed from the top view for samples annealed at 480°C. The cross-sectional view reveals the presence of some voids below the top surface. Pinholes do appear for samples annealed at 540°C and 600°C. These pinholes will allow direct access of the electrolyte to the FTO electrode and potentially lead to low resistance shunting losses and recombination losses through HER back-reaction as a result of accumulation of the photogenerated holes at the $CuBi_2O_4$/FTO interphase, lowering the solar-to-hydrogen (STH) efficiency.[66] The SEM images suggest the origin of the pinhole formation is the annealing step leading to grain growth and the formation of granules.[67, 68] Particle size quantification analysis using Image J confirms that larger granules seem to form at the expense of the smaller ones, indicating grain growth consistent with the Ostwald ripening mechanism see **Figure S7** in the Supplementary Information. The exposed FTO surface is estimated using a histogram-based intensity thresholding algorithm, determining the relative pinhole area at 16 and 26%, respectively, for annealing at 540°C and 600°C. AFM measurements reveal relatively small root mean square roughness values of 14-20 nm when compared to the total the film thickness of +-170 nm. Hence, we argue that the grain growth mainly occurs laterally and the effective CBO surface area ($cm^2_{eff} \cdot cm^{-2}_{geometric}$) can be estimated from the AFM surface area ($cm^2 \cdot cm^{-2}_{geometric}$) and CBO surface coverage (%) estimated from SEM, see **Table 2**.

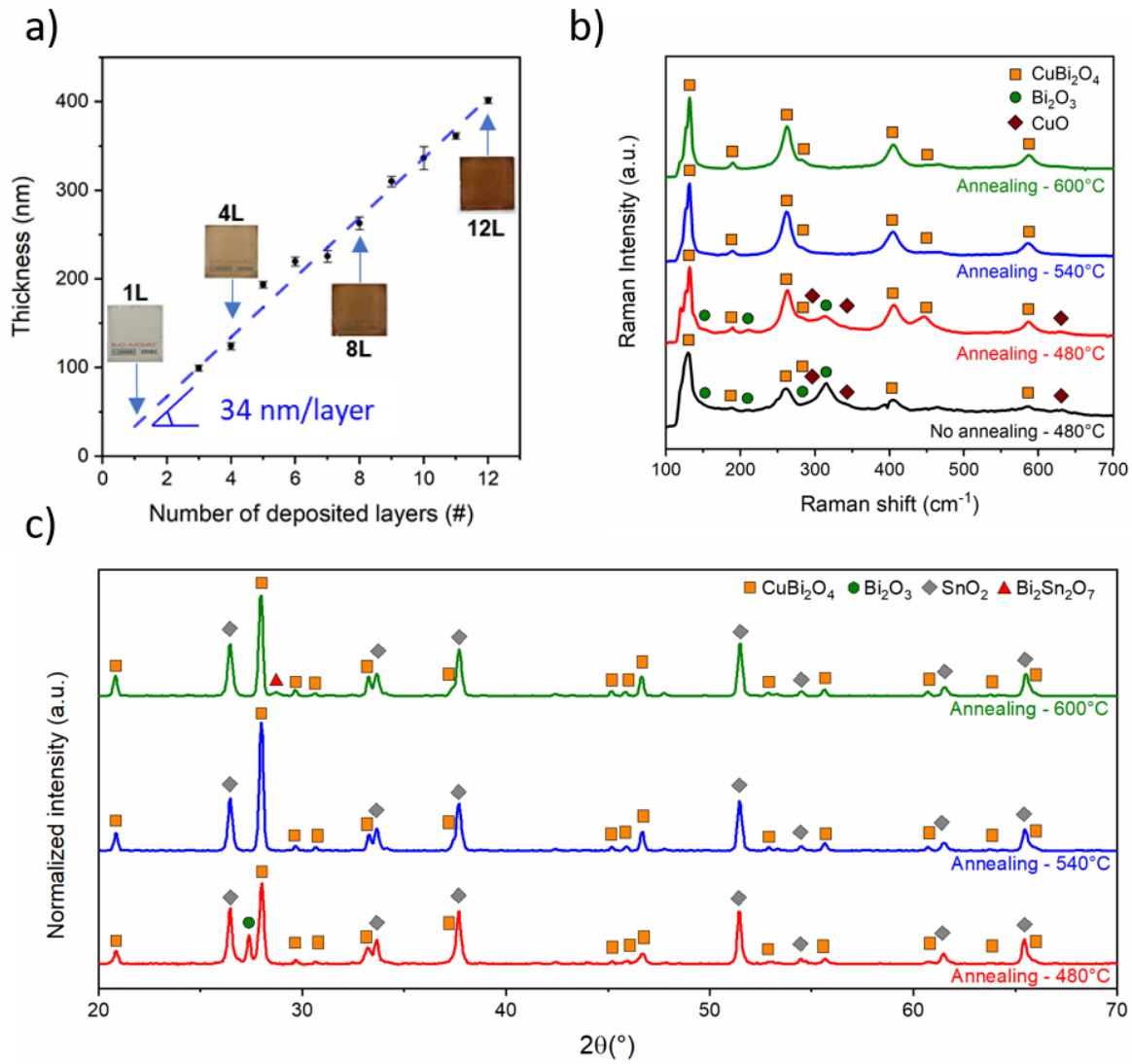

Figure 3. a) Thickness of the Cu/Bi oxide films in function of the number of deposited layers. (b) Raman spectra of five layers (±170 nm) of the Cu/Bi oxide deposited on the FTO/glass substrates before and after annealing at selected temperatures for two hours in ambient. The $CuBi_2O_4$, Bi_2O_3, and CuO Raman vibrations are given in orange squares, green circles, and brown diamonds respectively.[59, 60, 64] c) X-ray diffractograms of the five layers (±170 nm) of the Cu/Bi oxide deposited on the FTO/glass substrates before and after annealing. The intensities are normalized to the (110) diffraction peak of the F:SnO_2 TCO. The $CuBi_2O_4$ (COD no. 96-100-8477), Bi_2O_3 (COD no. 96-901-2547), $Bi_2Sn_2O_7$ (COD no. 96-432-6954), and SnO_2 (COD no. 96-900-7434) diffraction peaks are given in orange squares, green circles, red triangles, and grey diamonds respectively.[53, 59-64]

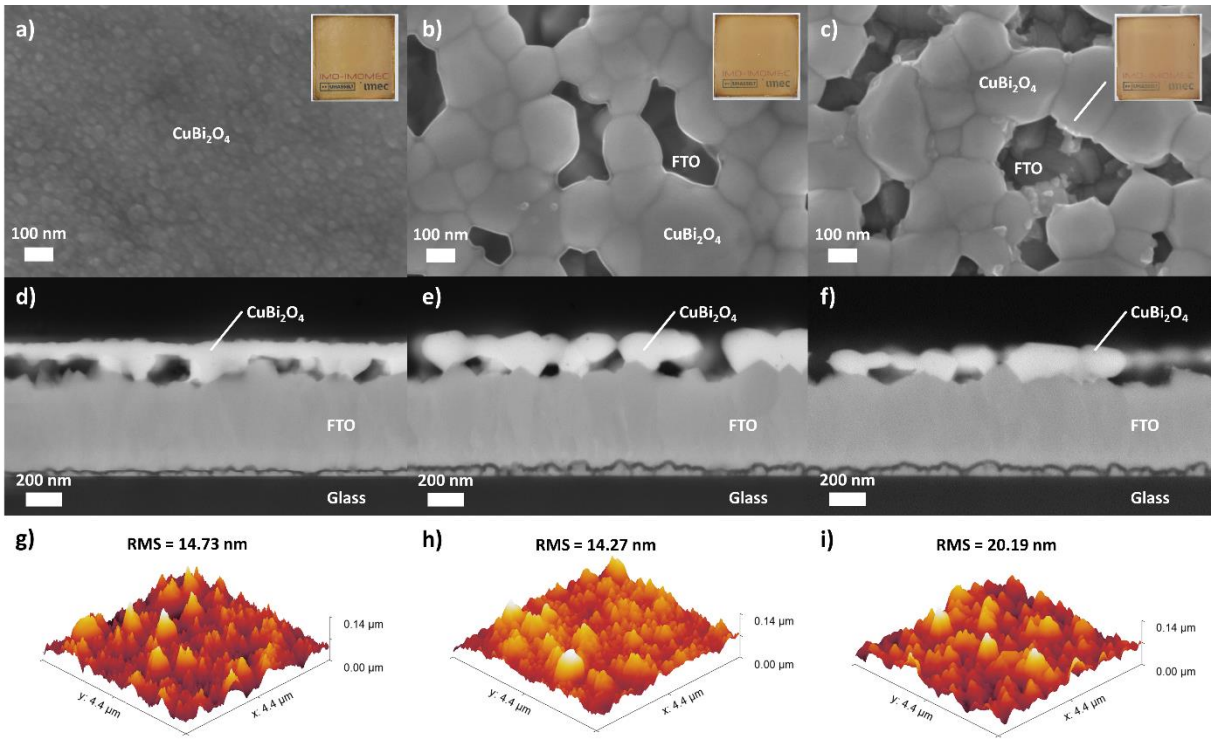

Figure 4. SEM (top) with optical image in the inset, cross-sectional SEM (middle) and corresponding AFM (right) images of the deposited CBO (5 layers) on FTO/glass substrate annealed at 480°C (a,d,g), 540°C (b,e,h), 600°C (c,f,i) respectively. In lens secondary electron images reveal the morphology of the deposited CBO film. The insets are the optical photographs of the films to show the impact on the optical transparency.

The influence of the annealing temperature on the formation of crystalline phases in the five-layer model Cu/Bi oxide film is evaluated by means of X-ray diffraction, see **Figure 3c**. The main phase in either film is evidently the CBO kusachiite phase.[53, 61, 62] Again, a small amount of monoclinic Bi_2O_3 bismite phase is detected in the film annealed at 480°C but vanishes above this annealing temperature.[65] No crystalline CuO could be detected regardless of annealing temperature. Interestingly, annealing at 600°C seems to lead to the formation of a small $Bi_2Sn_2O_7$ side-phase, indicating the reaction of the FTO film with unreacted Bi_2O_3 bismite. ICP-AES measurements were carried out after the dissolution of the CBO films with 5 wt% nitric acid, similarly to the powder samples, see **Table 2**. The stoichiometry was maintained throughout the thermal treatment, confirming no loss of Cu or Bi. However, in contrary to the powder samples, weak Raman vibrations related to CuO phase were detected, most notably at the B_g vibration mode at 640 cm^{-1}, see **Figure 3b**.[64] The vibrations correlated to Bi_2O_3 and CuO vanish upon annealing above 480°C, consistent with the XRD results. This supports our hypothesis that Bi_2O_3 and CuO side-phases form as intermediates upon calcination and are consumed to form $CuBi_2O_4$ upon annealing.

The results above confirm the ability of the proposed pH neutral aqueous solution-gel route to deposit a nearly phase-pure crystalline CBO film with desirable thickness. No degradation of the previously deposited layers is observed, e.g. by preferential leaching of either of the two metal ions or dissolution of the whole layer. Finally, the opto-electronic properties of the CBO films are examined before the evaluation of their performance as a photocathode.

Table 2. Elemental analysis by ICP-AES of the liquid multi metal precursor (MuMI), non-annealed (NA), and annealed (at select temperatures, i.e. 480, 540, or 600°C) five-layer (±170 nm) films of the multi

metal oxide deposited on the FTO/glass substrates. The bandgap *Eg* (eV) was determined from a seven-layer (± 163 nm) films of the multi metal oxide deposited on the quartz substrate. The effective surface area S_{CBO} ($cm^2_{eff}/cm^2_{geometric}$) of the $CuBi_2O_4$film is evaluated by the sample surface area S_{tot} ($cm^2_{eff}/cm^2_{geometric}$) obtained from AFM and $CuBi_2O_4$ surface coverage (%) from SEM. Similarly, the exposed surface area S_{FTO} ($cm^2_{eff}/cm^2_{geometric}$) of FTO is given. The flat-band potential ϕ_{FB} (V vs. RHE at pH 6.85) and charge carrier density N_A (10^{18} cm^{-3}) are estimated from the Mott-Schottky measurements.

Sample	ICP-AES	UV-VIS	AFM/SEM			Mott-Schottky	
Calc. T (°C)	Bi/Cu	E_g (eV)	S_{tot}	S_{FTO}	S_{CBO}	φ_{FB} (V vs. RHE)	N_A (10^{18} cm^{-3})
MuMI	2.01	N/A	N/A	N/A	N/A	N/A	N/A
NA	2.01	1.85	N/A	N/A	N/A	N/A	N/A
480	2.02	1.88	1.018	0	1.018	1.40 ± 0.02	35.2 ± 0.07
540	2.03	1.85	1.0220	0.163	0.858	1.42 ± 0.01	31.8 ± 0.05
600	2.03	1.87	1.0316	0.268	0.763	1.404 ± 0.001	12.7 ± 0.01

The bandgap of the semiconducting CBO film is determined by means of UV-Vis spectroscopy. To this end, CBO with various thicknesses (# layers) is deposited on fused silica substrates with an identical multimetal ion precursor and thermal treatment, i.e. calcination and two hours annealing at 540°C, as described above. See **Figure S8** for the optical photographs and **Figure S9** for the thickness relation in the Supplementary Information. The linear relationship between the film thickness and the number of depositions still holds on the fused silica substrate but with an overall thinner layer per deposition, i.e. ±25 nm per layer (compared against ±34 nm/layer on FTO). We argue this can be attributed to the lower surface roughness of the fused silica substrate compared to the FTO/glass substrate. Hence, the five-layer model film of CBO on the FTO/glass substrate is comparable in thickness to the seven-layer film of the CBO on the fused silica substrate, which is selected as the model sample for optical measurements. The absorptance increases gradually with increasing film thickness, see **Figure 5a**. evident by the reduced optical transmittance upon increasing film thickness, see **Figure S8** in the Supplementary Information. The absorption coefficient α is then used to calculate the band gap energy *Eg* using the Tauc method.[69] According to Equation 8, with *A* a constant, the bandgap value can be obtained by the intercepts of linear extrapolation of $(\alpha h\nu)^{1/n}$ *vs* $h\nu$ plot on the energy axis.[70]

Equation 8 $$\alpha h\nu = A\left(h\nu - E_g\right)^n$$

CBO is known to be a narrow bandgap p-type semiconductor with a direct allowed transition with a bandgap E_g around 1.6 to 1.9 eV.[20, 22, 23, 27] Hence n is taken as ½ for direct allowed transitions with hν (eV) the energy of the photon. The bandgap of films of variable thickness, see **Table S2** in Supplementary Information, varies between 1.86 and 1.91 eV with no consistent trend. The Tauc-plot of the model seven-layer film (± 163 nm) of the CBO deposited and annealed at 540°C for two hours on the fused silica substrate is given below in **Figure 5b,** alongside Tauc plots of the non-annealed and annealed seven-layer films at 480°C and 600°C to study the effect of the annealing temperature. No significant influence of the annealing temperature on the bandgap was found, with the bandgap varying between 1.85 and 1.89 eV. Hence, we conclude that apparent variation originates from the experimental error of the measurement and fit rather than intrinsic shifting of the valence and conduction band levels. The bandgap is somewhat higher than usually reported for CBO.[20, 22, 23, 27]

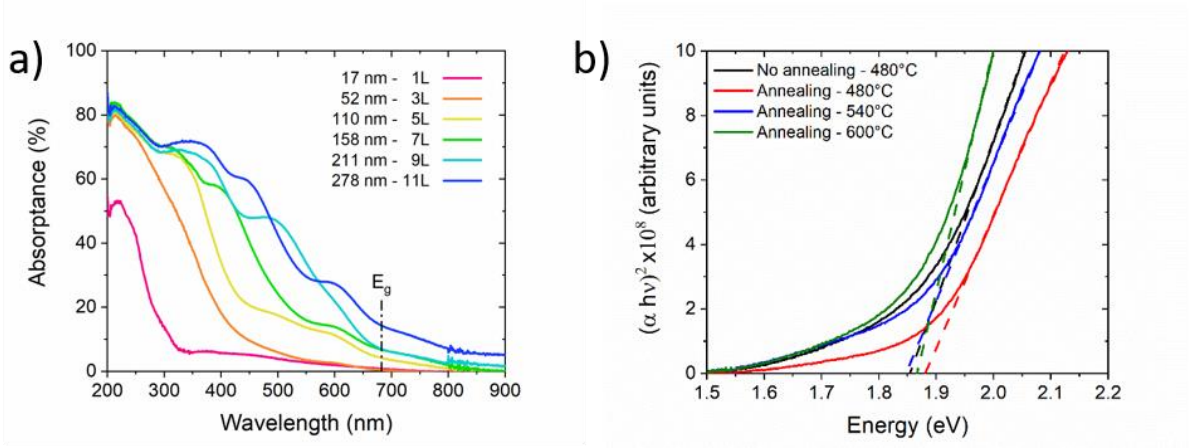

Figure 5. a) Absorptance plot vs thickness of the CBO films of selected thicknesses on fused silica substrates annealed at 540°C for two hours. b) Tauc plots of the model seven-layer CBO on fused silica substrates (non-)annealed at 480°C, 540°C, or 600°C for two hours.

The ability of the deposited CBO to reduce protons to form hydrogen depends not only on its capability to absorb suitable photons, but the position of the conduction band edge as well. Therefore, the flat band potential ϕ_{FB} and the acceptor density N_A of the prepared p-type $CuBi_2O_4$ is determined by means of Mott-Schottky measurements. The model five-layer CBO on FTO/glass is utilized. The Mott-Schottky measurements of the annealed films are given in **Figure 6**, the extracted data in **Table 2**, and the Nyquist plot of the sample annealed at 540°C is given in **Figure S10 i**n the Supplementary Information. The negative slope between the depletion and accumulation region confirms the p-type character of the deposited CBO films. The Equation 4 given in the experimental section is utilized to estimate the flat band potential ϕ_{FB} and the acceptor density N_A.[2, 54, 55] The flat band potential ϕ_{FB} is independent of the annealing temperature and found consistently around 1.4 V vs. RHE (at pH 6.85), agreeing well with values reported in literature.[20, 27] Instead, the acceptor density decreased from $3.52 \cdot 10^{19}$ cm^{-3} to $1.27 \cdot 10^{19}$ cm^{-3} upon increasing the annealing temperature as evident from the increasing slope. The acceptor density N_A is somewhat higher than reported in literature for stoichiometric $CuBi_2O_4$, and could be due to a higher content of copper vacancies in the CBO and/or the impact of the Bi_2O_3 and CuO side-phases.[20, 27] A striking correlation is found between the decrease in acceptor density N_A and the disappearance of Bi_2O_3 and CuO XRD and Raman signals with higher annealing temperatures, indicating that a significant amount of CuO is left unreacted in the deposited film annealed at 480°C.

The valence band edge's potential U_V is slightly more positive (as expected for a p-type semiconductor) than the flat band potential ϕ_{FB}, or the Fermi level potential U_F, at approximately 1.5 V vs. RHE, as calculated using Equation 5 and Equation 6 in the experimental section and assuming a valence band density of states N_V of $5 \cdot 10^{19}$ cm^{-3} as suggested by Van de Krol *et al.*[20, 54] Subsequently, the conduction band edge's potential U_C is found at approximately -0.4 V vs. RHE at pH 6.85, sufficiently negative to allow hydrogen evolution, see **Figure 6**. The space charge layer thickness D can be estimated at 14 nm at 0.6 V vs. RHE for the CBO annealed at 480°C and 540°C, and 23 nm for the CBO annealed at 600°C, using Equation 5 in the experimental section.[54]

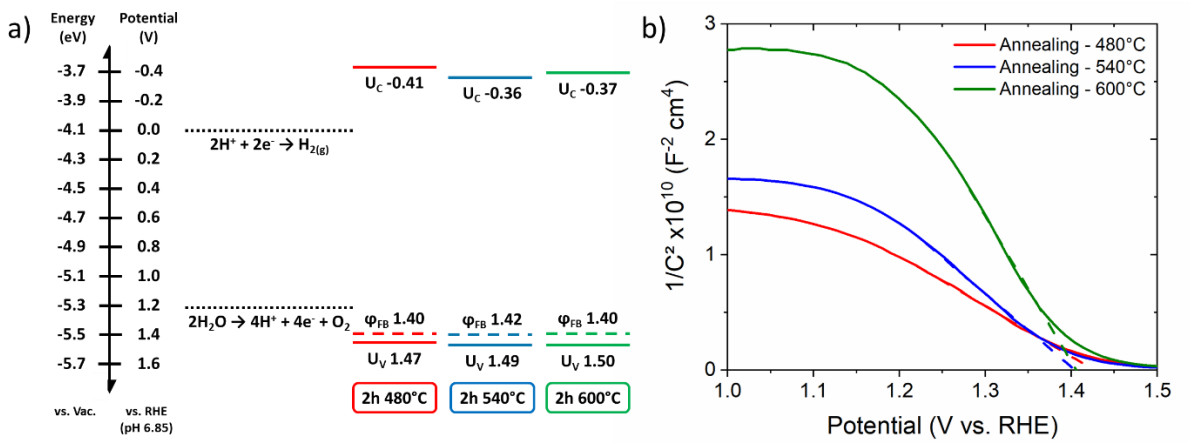

Figure 6. a) Energy level (eV vs. Vacuum) and electrochemical potential diagrams (V vs. RHE) and b) Mott-Schottky plots for the five-layer model CBO films annealed at 480°C, 540°C, or 600°C for two hours in ambient.

The photoelectrochemical performance of the CBO films annealed at 540°C is evaluated by the photocurrent analysis with a phosphate buffer (0.2M, pH 6.85, 0.3M K_2SO_4). Hydrogen peroxide was used as an electron scavenger to limit the influence of the reduction kinetics on the observed currents.[20] However, it has to be taken into account that hydrogen peroxide leads to current doubling by injection of a hole into the valence band.[20] The influence of the CBO thickness on the observed photocurrents is shown in **Figure 7** at selected bias potentials. An optimum is found at four layers of CBO deposition, i.e. approx. 135 nm, with the current density reaching -0.62, -0.82, -1.02 mA/cm² at 0.8, 0.6, and 0.4 V vs. RHE respectively with the use of H_2O_2 as the electron scavenger. These values agree well with those observed by the group of Van de Krol upon the deposition of CBO using organic solvents.[20] The low absorptivity of the CBO film would preferably require larger film thicknesses but difficult charge carrier transport presumably limits the kinetics. It is well known that the hole carrier diffusion length and lifetime are an issue for this material.[20, 27] The dark and light currents of the optimal sample, i.e. four-layer film, are also shown below in **Figure 7**. A significant dark current is observed below 0.4 V vs. RHE, likely to originate from photo corrosion. The onset cathodic photocurrent is found to be above 1 V vs. RHE, which can be ascribed to the high potential Fermi level of the deposited CBO.

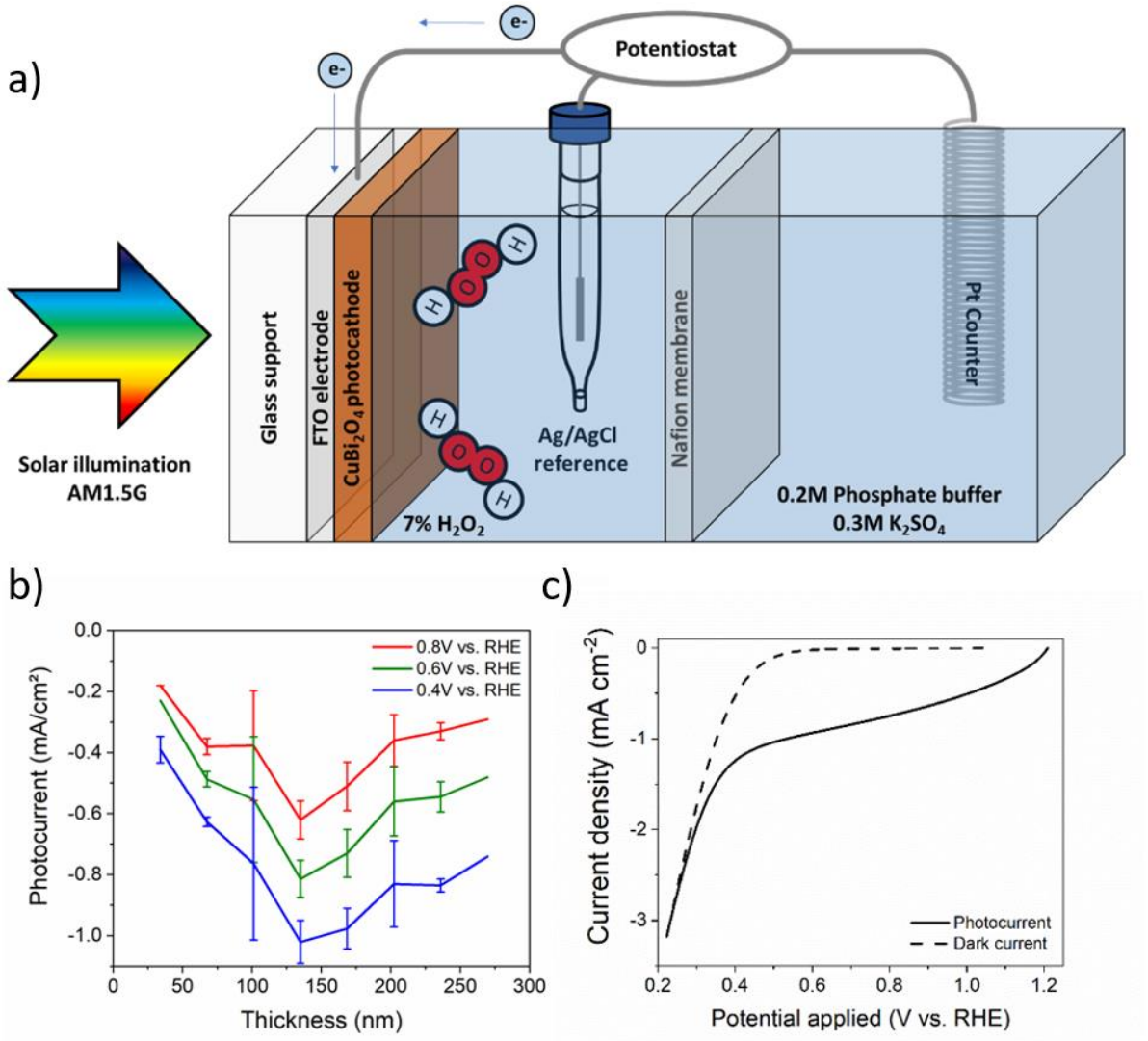

Figure 7. a) The setup of the photoelectrochemical cell with the $CuBi_2O_4$ photocathode deposited on FTO coated glass substrates, platinum counter electrode and the Ag/AgCl reference electrode. The photocathode is illuminated from the backside by a LED solar simulator (Redox.me AAA). b) The photocurrent at selected applied bias in function of the CBO's thickness annealed at 540°C. c) Observed currents under dark and light conditions for the optimal four-layer CBO annealed at 540°C.

Conclusions & outlook

This work demonstrates a flexible and pH-neutral solution-gel route which allows solution-processing of $CuBi_2O_4$. The complexation of the Bi^{3+} cation with the citrato- and monoethanolamine-based ligands extends the solubility and allows deposition at neutral pH. Hence, the proposed route offers unprecedented flexibility with pH sensitive materials. This allowed us to deposit multiple films of $CuBi_2O_4$ without any undesirable effects on the previous layer, often seen in the case of electroplating upon lifting the cathodic current. The oxidative thermal treatment is able to remove the organics and allow the formation of nearly phase-pure p-type $CuBi_2O_4$ with a bandgap of approximately 1.85 eV. Raman spectroscopy, XRD, and Mott-Schottky measurements suggest that CuO residual-phase plays an important role in governing the Cu-deficiency in $CuBi_2O_4$ thin films. ICP-AES confirms the presence as the Bi/Cu ratio is stoichiometric. Annealing converts the minor CuO and Bi_2O_3 side-phases into the desired stoichiometric CBO but grain growth causes a slight contraction of the uniform layer into

interconnected granules without a significant increase of exposed surface area. An optimum in performance is found at a thickness of 135 nm, with photocurrent density reaching 1.02 mA/cm² at 0.4 V vs. RHE. Keeping in mind the low absorption coefficient α, an enhanced performance can be expected from thicker films yet it is hindered by the well-known low hole diffusion length of the CBO material.[2, 20] Light management through the use of back reflectors could be an effective solution. Looking forward, the proposed solution-gel route can easily be adapted to include dopants, e.g. with Ag, to address the (photo)corrosion issues.[23] Another route would be to implement nanostructuring to disentangle the optical and electrical path lengths, or coat the CBO on hole conducting layers such a NiO for better hole extraction at the FTO back contact and suppress the recombination losses.[66] Ultimately, fully aqueous solution-processed photoelectrode is envisioned.

Acknowledgements

We would like to thank TNO for their financial support and acknowledge help by An-Sofie Kelchtermans for ICP-AES measurements, Willem Vercruysse and Amine Lataf for Elemental CHNS analysis, Jonas Mercken for borrowing the DSLR camera, Aleksandra Ciesielska, Femke Derison, and Giovanni Sementilli for the help with sample preparation. Sudhanshu Shukla acknowledges funding from the European Union's Horizon Europe program under the Marie Skłodowska-Curie Grant Agreement No. 101067667. The work has received funding from the Belgian federal government through the Energy Transition Fund T-REX project. The work was supported by the Flemish Government 'Vlaamse Veerkracht' project VV021/07 'UHasselt Green Hydrogen Lab'.

References

1. Taibi, E.; Miranda, R.; Carmo, M.; Blanco, H., Green hydrogen cost reduction. **2020**.
2. Van de Krol, R.; Grätzel, M., *Photoelectrochemical hydrogen production*. Springer: 2012; Vol. 90.
3. Jiang, C.; Moniz, S. J. A.; Wang, A.; Zhang, T.; Tang, J., Photoelectrochemical devices for solar water splitting – materials and challenges. *Chemical Society Reviews* **2017,** *46* (15), 4645-4660.
4. Moon, C.; Shin, B., Review on light absorbing materials for unassisted photoelectrochemical water splitting and systematic classifications of device architectures. *Discover Materials* **2022,** *2* (1).
5. Cheng, W.-H.; Richter, M. H.; May, M. M.; Ohlmann, J.; Lackner, D.; Dimroth, F.; Hannappel, T.; Atwater, H. A.; Lewerenz, H.-J., Monolithic Photoelectrochemical Device for Direct Water Splitting with 19% Efficiency. *ACS Energy Letters* **2018,** *3* (8), 1795-1800.
6. Young, J. L.; Steiner, M. A.; Döscher, H.; France, R. M.; Turner, J. A.; Deutsch, Todd G., Direct solar-to-hydrogen conversion via inverted metamorphic multi-junction semiconductor architectures. *Nature Energy* **2017,** *2* (4).
7. Verlage, E.; Hu, S.; Liu, R.; Jones, R. J. R.; Sun, K.; Xiang, C.; Lewis, N. S.; Atwater, H. A., A monolithically integrated, intrinsically safe, 10% efficient, solar-driven water-splitting system based on active, stable earth-abundant electrocatalysts in conjunction with tandem III–V light absorbers protected by amorphous TiO2 films. *Energy & Environmental Science* **2015,** *8* (11), 3166-3172.
8. Koo, B.; Kim, D.; Boonmongkolras, P.; Pae, S. R.; Byun, S.; Kim, J.; Lee, J. H.; Kim, D. H.; Kim, S.; Ahn, B. T.; Nam, S.-W.; Shin, B., Unassisted Water Splitting Exceeding 9% Solar-to-Hydrogen Conversion Efficiency by Cu(In, Ga)(S, Se)2 Photocathode with Modified Surface Band Structure and Halide Perovskite Solar Cell. *ACS Applied Energy Materials* **2020,** *3* (3), 2296-2303.
9. Gurudayal; Sabba, D.; Kumar, M. H.; Wong, L. H.; Barber, J.; Gratzel, M.; Mathews, N., Perovskite-Hematite Tandem Cells for Efficient Overall Solar Driven Water Splitting. *Nano Lett* **2015,** *15* (6), 3833-9.
10. Liang, G.; Liu, T.; Ishaq, M.; Chen, Z.; Tang, R.; Zheng, Z.; Su, Z.; Fan, P.; Zhang, X.; Chen, S., Heterojunction interface engineering enabling high onset potential in Sb2Se3/CdS photocathodes for efficient solar hydrogen production. *Chemical Engineering Journal* **2022,** *431*, 133359.
11. Liang, G.; Li, Z.; Ishaq, M.; Zheng, Z.; Su, Z.; Ma, H.; Zhang, X.; Fan, P.; Chen, S., Charge Separation Enhancement Enables Record Photocurrent Density in Cu2ZnSn (S, Se) 4 Photocathodes for Efficient Solar Hydrogen Production. *Advanced Energy Materials* **2023**, 2300215.
12. Chen, S.; Liu, T.; Chen, M.; Ishaq, M.; Tang, R.; Zheng, Z.; Su, Z.; Li, X.; Qiao, X.; Fan, P., Crystal growth promotion and interface optimization enable highly efficient Sb2Se3 photocathodes for solar hydrogen evolution. *Nano Energy* **2022,** *99*, 107417.
13. Chen, S.; Liu, T.; Zheng, Z.; Ishaq, M.; Liang, G.; Fan, P.; Chen, T.; Tang, J., Recent progress and perspectives on Sb2Se3-based photocathodes for solar hydrogen production via photoelectrochemical water splitting. *Journal of Energy Chemistry* **2022,** *67*, 508-523.
14. Yang, W.; Park, J.; Kwon, H.-C.; Hutter, O. S.; Phillips, L. J.; Tan, J.; Lee, H.; Lee, J.; Tilley, S. D.; Major, J. D.; Moon, J., Solar water splitting exceeding 10% efficiency via low-cost Sb2Se3 photocathodes coupled with semitransparent perovskite photovoltaics. *Energy & Environmental Science* **2020,** *13* (11), 4362-4370.
15. Prabhakar, R. R.; Septina, W.; Siol, S.; Moehl, T.; Wick-Joliat, R.; Tilley, S. D., Photocorrosion-resistant Sb2Se3photocathodes with earth abundant MoSxhydrogen evolution catalyst. *Journal of Materials Chemistry A* **2017,** *5* (44), 23139-23145.
16. Wu, X.; Zhao, W.; Hu, Y.; Xiao, G.; Ni, H.; Ikeda, S.; Ng, Y.; Jiang, F., Research on the Influence of the Interfacial Properties Between a Cu3BiS3 Film and an InxCd1−xS Buffer Layer for Photoelectrochemical Water Splitting. *Advanced Science* **2022,** *9* (33), 2204029.

17. Huang, D.; Li, L.; Wang, K.; Li, Y.; Feng, K.; Jiang, F., Wittichenite semiconductor of Cu3BiS3 films for efficient hydrogen evolution from solar driven photoelectrochemical water splitting. *Nature Communications* **2021,** *12* (1), 3795.
18. Zhao, Y.; Yu, Z.; Hu, J.; Zheng, Z.; Ma, H.; Sun, K.; Hao, X.; Liang, G.; Fan, P.; Zhang, X.; Su, Z., Over 12% efficient kesterite solar cell via back interface engineering. *Journal of Energy Chemistry* **2022,** *75*, 321-329.
19. Fan, P.; Lin, J.; Hu, J.; Yu, Z.; Zhao, Y.; Chen, S.; Zheng, Z.; Luo, J.; Liang, G.; Su, Z., Over 10% Efficient Cu2CdSnS4 Solar Cells Fabricated from Optimized Sulfurization. *Advanced Functional Materials* **2022,** *32* (45), 2207470.
20. Berglund, S. P.; Abdi, F. F.; Bogdanoff, P.; Chemseddine, A.; Friedrich, D.; van de Krol, R., Comprehensive Evaluation of CuBi2O4 as a Photocathode Material for Photoelectrochemical Water Splitting. *Chemistry of Materials* **2016,** *28* (12), 4231-4242.
21. Gottesman, R.; Song, A.; Levine, I.; Krause, M.; Islam, A. T. M. N.; Abou-Ras, D.; Dittrich, T.; van de Krol, R.; Chemseddine, A., Pure CuBi2O4 Photoelectrodes with Increased Stability by Rapid Thermal Processing of Bi2O3/CuO Grown by Pulsed Laser Deposition. *Advanced Functional Materials* **2020,** *30* (21), 1910832.
22. Hahn, N. T.; Holmberg, V. C.; Korgel, B. A.; Mullins, C. B., Electrochemical synthesis and characterization of p-CuBi2O4 thin film photocathodes. *The Journal of Physical Chemistry C* **2012,** *116* (10), 6459-6466.
23. Kang, D.; Hill, J. C.; Park, Y.; Choi, K.-S., Photoelectrochemical Properties and Photostabilities of High Surface Area CuBi2O4 and Ag-Doped CuBi2O4 Photocathodes. *Chemistry of Materials* **2016,** *28* (12), 4331-4340.
24. Lee, J.; Yoon, H.; Choi, K. S.; Kim, S.; Seo, S.; Song, J.; Choi, B.-U.; Ryu, J.; Ryu, S.; Oh, J.; Jeon, C.; Lee, S., Template Engineering of CuBi2O4 Single-Crystal Thin Film Photocathodes. *Small* **2020,** *16* (39), 2002429.
25. Oropeza, F. E.; Dzade, N. Y.; Pons-Martí, A.; Yang, Z.; Zhang, K. H. L.; de Leeuw, N. H.; Hensen, E. J. M.; Hofmann, J. P., Electronic Structure and Interface Energetics of CuBi2O4 Photoelectrodes. *The Journal of Physical Chemistry C* **2020,** *124* (41), 22416-22425.
26. Patil, R.; Kelkar, S.; Naphade, R.; Ogale, S., Low temperature grown CuBi2O4 with flower morphology and its composite with CuO nanosheets for photoelectrochemical water splitting. *Journal of Materials Chemistry A* **2014,** *2* (10), 3661-3668.
27. Wang, F.; Septina, W.; Chemseddine, A.; Abdi, F. F.; Friedrich, D.; Bogdanoff, P.; van de Krol, R.; Tilley, S. D.; Berglund, S. P., Gradient self-doped CuBi2O4 with highly improved charge separation efficiency. *Journal of the American Chemical Society* **2017,** *139* (42), 15094-15103.
28. Wang, Y.; Liu, C.; Zhang, Y.; Meng, W.; Yu, B.; Pu, S.; Yuan, D.; Qi, F.; Xu, B.; Chu, W., Sulfate radical-based photo-Fenton reaction derived by CuBi2O4 and its composites with α-Bi2O3 under visible light irradiation: Catalyst fabrication, performance and reaction mechanism. *Applied Catalysis B: Environmental* **2018,** *235*, 264-273.
29. Song, A.; Bogdanoff, P.; Esau, A.; Ahmet, I. Y.; Levine, I.; Dittrich, T.; Unold, T.; van de Krol, R.; Berglund, S. P., Assessment of a W:BiVO4–CuBi2O4Tandem Photoelectrochemical Cell for Overall Solar Water Splitting. *ACS Applied Materials & Interfaces* **2020,** *12* (12), 13959-13970.
30. Cooper, J. K.; Zhang, Z.; Roychoudhury, S.; Jiang, C.-M.; Gul, S.; Liu, Y.-S.; Dhall, R.; Ceballos, A.; Yano, J.; Prendergast, D.; Reyes-Lillo, S. E., CuBi2O4: Electronic Structure, Optical Properties, and Photoelectrochemical Performance Limitations of the Photocathode. *Chemistry of Materials* **2021,** *33* (3), 934-945.
31. Abdulkarem, A. M.; Li, J.; Aref, A. A.; Ren, L.; Elssfah, E. M.; Wang, H.; Ge, Y.; Yu, Y., CuBi2O4 single crystal nanorods prepared by hydrothermal method: Growth mechanism and optical properties. *Materials Research Bulletin* **2011,** *46* (9), 1443-1450.
32. Wang, F.; Yang, H.; Zhang, H.; Jiang, J., Growth process and enhanced photocatalytic performance of CuBi2O4 hierarchical microcuboids decorated with AuAg alloy nanoparticles. *Journal of Materials Science: Materials in Electronics* **2018,** *29* (2), 1304-1316.

33. Duployer, B.; Tenailleau, C.; Thimont, Y.; Lenormand, P.; Barnabé, A.; Presmanes, L., Preparation and study of CuBi2O4 thin films by RF magnetron sputtering. *Materials Research Bulletin* **2020,** *130*, 110940.
34. Astle, M. J., CRC Han book. **1974**.
35. Agency, E. C. Water solubility of bismuth citrate. https://echa.europa.eu/registration-dossier/-/registered-dossier/11383/4/9#:~:text=The%20water%20solubility%20of%20bismuth,10.97%20to%2053.81%20mg%2FL.
36. Hardy, A.; Vanhoyland, G.; Geuzens, E.; Van Bael, M. K.; Mullens, J.; Van Poucke, L. C.; D'Haen, J., Gel Structure, Gel Decomposition and Phase Formation Mechanisms in the Aqueous Solution–Gel Route to Lanthanum Substituted Bismuth Titanate. *Journal of Sol-Gel Science and Technology* **2005,** *33* (3), 283-298.
37. Jiang, S.; Huang, Y.-H.; Luo, F.; Du, N.; Yan, C.-H., Synthesis of bismuth with various morphologies by electrodeposition. *Inorganic Chemistry Communications* **2003,** *6* (6), 781-785.
38. Kang, D.; Park, Y.; Hill, J. C.; Choi, K.-S., Preparation of Bi-Based Ternary Oxide Photoanodes BiVO4, Bi2WO6, and Bi2Mo3O12 Using Dendritic Bi Metal Electrodes. *The Journal of Physical Chemistry Letters* **2014,** *5* (17), 2994-2999.
39. Das, B.; Lathabai, D. In *Sol-Gel Synthesis and Structure-Property Relations in ZnxCu1-xBi2O4 (0≤ x≤ 0.6) Spinels*, Solid State Phenomena, Trans Tech Publ: 2006; pp 31-34.
40. Ma, K.; Pierre, A. C., Sol-gel processing of high-Tc superconductors in the Bi–(Pb)–Sr–Ca–Cu–O system. *Journal of materials research* **1992,** *7* (6), 1328-1335.
41. De Dobbelaere, C.; Mullens, J.; Hardy, A.; Van Bael, M. K., Thermal decomposition and spectroscopic investigation of a new aqueous glycolato(-peroxo) Ti(IV) solution–gel precursor. *Thermochimica Acta* **2011,** *520* (1), 121-133.
42. Hardy, A.; D'Haen, J.; Van Bael, M. K.; Mullens, J., An aqueous solution–gel citratoperoxo–Ti(IV) precursor: synthesis, gelation, thermo-oxidative decomposition and oxide crystallization. *Journal of Sol-Gel Science and Technology* **2007,** *44* (1), 65-74.
43. Hardy, A.; Mondelaers, D.; Van Bael, M. K.; Mullens, J.; Van Poucke, L. C.; Vanhoyland, G.; D'Haen, J., Synthesis of (Bi,La)4Ti3O12 by a new aqueous solution-gel route. *Journal of the European Ceramic Society* **2004,** *24* (6), 905-909.
44. Hardy, A.; Mondelaers, D.; Vanhoyland, G.; Van Bael, M. K.; Mullens, J.; Van Poucke, L. C., The Formation of Ferroelectric Bismuth Titanate (Bi4Ti3O12) from an Aqueous Metal-Chelate Gel. *Journal of Sol-Gel Science and Technology* **2003,** *26* (1), 1103-1107.
45. Hardy, A.; Van Elshocht, S.; Adelmann, C.; Conard, T.; Franquet, A.; Douhéret, O.; Haeldermans, I.; D'Haen, J.; De Gendt, S.; Caymax, M.; Heyns, M.; D'Olieslaeger, M.; Van Bael, M. K.; Mullens, J., Aqueous solution–gel preparation of ultrathin ZrO2 films for gate dielectric application. *Thin Solid Films* **2008,** *516* (23), 8343-8351.
46. Hardy, A.; Van Werde, K.; Vanhoyland, G.; Van Bael, M. K.; Mullens, J.; Van Poucke, L. C., Study of the decomposition of an aqueous metal–chelate gel precursor for (Bi,La)4Ti3O12 by means of TGA–FTIR, TGA–MS and HT-DRIFT. *Thermochimica Acta* **2003,** *397* (1), 143-153.
47. Ulu Okudur, F.; Mylavarapu, S. K.; Safari, M.; De Sloovere, D.; D'Haen, J.; Joos, B.; Kaliyappan, P.; Kelchtermans, A.-S.; Samyn, P.; Van Bael, M. K.; Hardy, A., LiNi0.5Mn1.5O4-δ (LNMO) as Co-free cathode for lithium ion batteries via solution-gel synthesis: Particle size and morphology investigation. *Journal of Alloys and Compounds* **2022,** *892*, 162175.
48. Van Bael, M. K.; Nelis, D.; Hardy, A.; Mondelaers, D.; Van Werde, K.; D'Haen, J.; Vanhoyland, G.; Van Den Rul, H.; Mullens, J.; Van Poucke, L. C.; Frederix, F.; Wouters, D. J., Aqueous Chemical Solution Deposition of Ferroelectric Thin Films. *Integrated Ferroelectrics* **2002,** *45* (1), 113-122.
49. Nelis, D.; Mondelaers, D.; Vanhoyland, G.; Hardy, A.; Werde, K. V.; Rul, H. V. d.; Bael, M. K. V.; Mullens, J.; Poucke, L. C. V.; D'Haen, J., Synthesis of strontium bismuth niobate (SrBi2Nb2O9) using an aqueous acetate–citrate precursor gel: thermal decomposition and phase formation. *Thermochimica Acta* **2005,** *426* (1), 39-48.

50. Marchal, W.; Longo, A.; Briois, V.; Van Hecke, K.; Elen, K.; Van Bael, M. K.; Hardy, A., Understanding the Importance of Cu(I) Intermediates in Self-Reducing Molecular Inks for Flexible Electronics. *Inorganic Chemistry* **2018,** *57* (24), 15205-15215.
51. Van Gompel, W. T. M.; Herckens, R.; Mertens, M.; Denis, P.-H.; Ruttens, B.; D'Haen, J.; Van Hecke, K.; Lutsen, L.; Vanderzande, D., Study on the Dynamics of Phase Formation and Degradation of 2D Layered Hybrid Perovskites and Low-dimensional Hybrids Containing Mono-functionalized Oligothiophene Cations. *ChemNanoMat* **2021,** *7* (9), 1013-1019.
52. Nečas, D.; Klapetek, P., Gwyddion: an open-source software for SPM data analysis. *Open Physics* **2012,** *10* (1), 181-188.
53. Klyndyuk, A.; Petrov, G.; Bashkirov, L.; Akimov, A.; Poluyan, A., Thermal stability and phase transformations in CuBi2O4. *Russian journal of inorganic chemistry* **1999,** *44* (1), 1-4.
54. Sze, S. M., *Physics of Semiconductor Devices*. Wiley: 1981.
55. Gomes, W. P.; Vanmaekelbergh, D., Impedance spectroscopy at semiconductor electrodes: Review and recent developments. *Electrochimica Acta* **1996,** *41* (7), 967-973.
56. Gómez‐Salces, S.; Aguado, F.; Valiente, R.; Rodríguez, F., Unraveling the coordination geometry of copper (II) ions in aqueous solution through absorption intensity. *Angewandte Chemie* **2012,** *124* (37), 9469-9472.
57. Zurbuchen, M. A.; Lettieri, J.; Fulk, S. J.; Jia, Y.; Carim, A. H.; Schlom, D. G.; Streiffer, S. K., Bismuth volatility effects on the perfection of SrBi2Nb2O9 and SrBi2Ta2O9 films. *Applied Physics Letters* **2003,** *82* (26), 4711-4713.
58. Barz, R.; Neumayer, D. A.; Majhi, P.; Wang, C.; Dey, S. K., Control of bismuth volatility in SBT by vanadium doping. *Integrated Ferroelectrics* **2001,** *39* (1-4), 61-71.
59. Popović, Z.; Kliche, G.; Cardona, M.; Liu, R., Vibrational properties of Bi 2 CuO 4. *Physical Review B* **1990,** *41* (6), 3824.
60. Narang, S.; Patel, N.; Kartha, V., Infrared and Raman spectral studies and normal modes of α-Bi2O3. *Journal of Molecular Structure* **1994,** *327* (2-3), 221-235.
61. Ong, E.; Kwei, G.; Robinson, R.; Ramakrishna, B.; Von Dreele, R., Long-range antiferromagnetic ordering in Bi 2 CuO 4. *Physical Review B* **1990,** *42* (7), 4255.
62. Henmi, C., Kusachiite, CuBi2O4, a new mineral from Fuka, Okayama Prefecture, Japan. *Mineralogical Magazine* **1995,** *59* (396), 545-548.
63. Schmidt, S.; Kubaski, E. T.; Volanti, D. P.; Sequinel, T.; Bezzon, V. D. N.; Beltrán, A.; Tebcherani, S. M.; Varela, J. A., Effect of pressure-assisted heat treatment on photoluminescence emission of α-Bi2O3 needles. *Inorganic Chemistry* **2015,** *54* (21), 10184-10191.
64. Murthy, P. S.; Venugopalan, V.; Arunya, D. D.; Dhara, S.; Pandiyan, R.; Tyagi, A. In *Antibiofilm activity of nano sized CuO*, International conference on nanoscience, engineering and technology (ICONSET 2011), IEEE: 2011; pp 580-583.
65. Gomis, O.; Manjón, F. J.; Rodríguez-Hernández, P.; Muñoz, A., Elastic and thermodynamic properties of α-Bi2O3 at high pressures: Study of mechanical and dynamical stability. *Journal of Physics and Chemistry of Solids* **2019,** *124*, 111-120.
66. Song, A.; Plate, P.; Chemseddine, A.; Wang, F.; Abdi, F. F.; Wollgarten, M.; van de Krol, R.; Berglund, S. P., Cu: NiO as a hole-selective back contact to improve the photoelectrochemical performance of CuBi 2 O 4 thin film photocathodes. *Journal of Materials Chemistry A* **2019,** *7* (15), 9183-9194.
67. Brune, H., Epitaxial Growth of Thin Films. In *Surface and Interface Science*, 2013; pp 421-492.
68. Michely, T.; Krug, J.; Michely, T.; Krug, J., Layer-By-Layer Growth and Growth Manipulation. *Islands, Mounds and Atoms* **2004**, 227-252.
69. Tauc, J., Optical properties and electronic structure of amorphous Ge and Si. *Materials Research Bulletin* **1968,** *3* (1), 37-46.
70. Makuła, P.; Pacia, M.; Macyk, W., How To Correctly Determine the Band Gap Energy of Modified Semiconductor Photocatalysts Based on UV–Vis Spectra. *The Journal of Physical Chemistry Letters* **2018,** *9* (23), 6814-6817.